

RESEARCH

Open Access



# Combination of rGO/S, N/TiO<sub>2</sub> for the enhancement of visible light-driven toluene photocatalytic degradation

Birgitta Narindri Rara Winayu, Wan-Hua Mao and Hsin Chu\*

## Abstract

Toluene is one type of common volatile organic compounds that is harmful to human health. Therefore, the degradation of toluene is critical to improving air quality value. Performance improvement of TiO<sub>2</sub>, a typically applied photocatalyst, has advantages in light absorption and electron transfer process. In this study, the TiO<sub>2</sub> catalyst was improved by the doping of reduced graphene oxide (rGO), sulfur, and nitrogen (S, N) elements. The highest toluene photocatalytic degradation was performed under the composition of 1wt%rGO/S<sub>0.05</sub>N<sub>0.1</sub>TiO<sub>2</sub>. Improvement in photocatalytic activity was achieved by higher specific surface area, formation of oxygen-containing functional group, and chemical defect structure. However, a higher amount of rGO addition creates the shielding effect and inhibits the light penetration. Moreover, the relative humidity and applied temperature influence the photocatalytic activity through the competitive adsorption or increase the collisions frequency, respectively. During the photocatalytic degradation using 0.1wt%rGO/S<sub>0.05</sub>N<sub>0.1</sub>TiO<sub>2</sub>, toluene will be converted into benzyl alcohol, benzaldehyde, benzoic acid, water, and carbon dioxide.

**Keywords:** Photocatalyst, Titanium oxide, Toluene, Non-metallic doping, Reduced graphene oxide

## 1 Introduction

An average 86–87% of human activities were spent in the indoor environment, thus the quality of air environment is important [1]. Various types of volatile organic compounds (VOCs), including toluene, have the potency to reduce the indoor air quality. Toluene as an aromatic hydrocarbon is commonly generated in various coal-burning products (from liquefaction process or coal aromatics) and other products like catalytic reforming products or the petroleum fractions after the steam cracking process [2]. Moreover, common daily human activities and materials like fuel combustion, application of cooking gas, wood furniture, cleaning agent, carpet, or pesticide also can be the source of toluene [3]. Toluene is

considered a carcinogenic agent and also harmful to the nervous system, liver, kidneys, and lungs, therefore, its removal is critical for human health [4].

Various strategies have been involved in the VOC control technologies like thermal, biological, or catalytic oxidation, condensation, adsorption, and absorption. However, most of the strategies have the potency to create the secondary pollutant, require high cost and energy, or are not effective for the low concentration pollutant [3, 5]. Photocatalytic degradation is a potential strategy for the removal of indoor air pollution with low cost and energy consumption, efficient for the low pollutant concentration. A widely applied photocatalyst, TiO<sub>2</sub>, has been implemented for the decomposition of organic compounds or even in the water remediation, super capacitor, porous adsorbent supports, and sensor devices [6]. However, under the visible-light irradiation, TiO<sub>2</sub> application was limited along with its

\*Correspondence: [chuhsin@mail.ncku.edu.tw](mailto:chuhsin@mail.ncku.edu.tw)

Department of Environmental Engineering, National Cheng Kung University, Tainan 70101, Taiwan



© The Author(s) 2022. **Open Access** This article is licensed under a Creative Commons Attribution 4.0 International License, which permits use, sharing, adaptation, distribution and reproduction in any medium or format, as long as you give appropriate credit to the original author(s) and the source, provide a link to the Creative Commons licence, and indicate if changes were made. The images or other third party material in this article are included in the article's Creative Commons licence, unless indicated otherwise in a credit line to the material. If material is not included in the article's Creative Commons licence and your intended use is not permitted by statutory regulation or exceeds the permitted use, you will need to obtain permission directly from the copyright holder. To view a copy of this licence, visit <http://creativecommons.org/licenses/by/4.0/>.

issue on the rate of photogenerated electron-hole pairs recombination.  $\text{TiO}_2$  has a wide bandgap of 3.2 eV, thus, the photocatalytic activity was driven by the UV illumination under the wavelength below 388 nm. Moreover, during the reaction, reduction of photocatalytic activity may occur due to the high recombination rate in electron-hole pairs that leads to the low electron concentration in conduction band. Therefore, interest has been gained for the improvement in  $\text{TiO}_2$  photocatalytic activity through modification [6].

Metal element doping on the  $\text{TiO}_2$  surface increases the capability to absorb visible lights through the formation of traps for photo-induced electron or holes that leads the electron to a reduction state during the photocatalytic process [7]. On the other hand, recombination inhibition for the  $\text{TiO}_2$  photogenerated electron-hole pair will be carried out by the non-metallic element doping [8]. Replacement of  $\text{TiO}_2$  lattice oxygen can be carried out by sulfur element as an anion. Furthermore, new energy states in  $\text{TiO}_2$  band gap may occur with the carbon element doping which will substitute the oxygen [9]. Moreover, the surface oxygen vacancies is achieved by the nitrogen element doping on  $\text{TiO}_2$  photocatalyst material [10].

$\text{TiO}_2$  doping with carbon material is a promising strategy due to its low cost, good conductivity property, and high absorbance of light that will improve the efficiency of pollutant photocatalytic degradation [11]. Furthermore, graphene has been observed for its enhancement on  $\text{TiO}_2$  photocatalyst through high electron mobility. The lower Fermi level of graphene compared to the minimum conduction band of  $\text{TiO}_2$  provides suitable utilization as the electron sink. Therefore, the interface charge separation and the inhibition of photogenerated electron-hole recombination will be facilitated by graphene. Moreover, in the  $\text{TiO}_2$ -graphene photocatalyst, the electron transfer from  $\text{TiO}_2$  surface to graphene causes a visible-light absorbance extension and the recombination inhibition of charge carrier [12].

This study observed the enhancement of  $\text{TiO}_2$  photocatalytic activity through doping of non-metallic elements (S, and N), and various concentrations of reduced graphene oxide (rGO). Toluene was chosen as the targeted pollutant for the study of indoor air pollution control using photocatalytic degradation. Moreover, the study of influence from various environmental conditions was also carried out along with the kinetic study and proposed degradation mechanism. Thus, this study provides comprehensive explanation including properties, performance, kinetics, and pollutant degradation mechanism of the  $\text{TiO}_2$  photocatalyst improvement via doping of non-metallic elements and low-cost material.

## 2 Experiments

### 2.1 Production of nanocomposite photocatalyst

Graphite oxide was prepared previously using the Hummer method [13]. Continuous stirring was applied for the mixture of graphite flakes (1 g),  $\text{NaNO}_3$  (0.5 g), and  $\text{H}_2\text{SO}_4$  (23 mL) under ice bath conditions for 1 h. 3 g  $\text{KMnO}_4$  was then slowly added under the stirring and the temperature that kept at below  $20^\circ\text{C}$  for 30 min before moving to the higher temperature water bath  $35^\circ\text{C}$  and continuing the stirring process for 24 h. Subsequently, water (46 mL) was added into the above mixture at  $95^\circ\text{C}$  during a period of 1 h. Finally, the suspension was diluted by adding 130 mL water and 12 mL  $\text{H}_2\text{O}_2$  (35 wt%) at room temperature and stirring was continued for another 30 min. The removal of un-exfoliated graphite oxide was carried out by repeated centrifugation-rinsing cycle using 5–10% HCl and water. The final product was then freeze-dried for storage.

Photocatalyst was prepared under the solvothermal method where titanium (IV) isopropoxide (TTIP) as the Ti-precursor, thiourea ( $\text{CH}_4\text{N}_2\text{S}$ ) as the sulfur-nitrogen-precursor (S, and N), and graphite oxide were used. S, and N elements were prepared with the amount of 5 mol% and 10 mol%, respectively for all various of observed graphite oxide concentration. Under the ultrasonic oscillation for 1 h, prepared graphite oxide (0.039 g) was added into ethanol (20 mL) for the formation of graphene oxide. Various concentrations of graphite oxide will be added in the ratio in the range of 0.01–1 wt%. Separately, 15 mL TTIP and 0.186 g thiourea were added into 20 mL ethanol. Both graphene oxide and TTIP-thiourea solution will be further mixed and supplemented by 100 mL deionized water under 30 min continuous stirring. Afterward, an adequate amount of nitric acid (65 wt%) was added to let the pH of the sol remain at 2 and be further stirred until the gel formed at  $70^\circ\text{C}$  for 30 min. The produced gel will be treated in Teflon-lined stainless steel and autoclaved for 12 h at the temperature of  $180^\circ\text{C}$ . Drying process at  $70^\circ\text{C}$  was applied as the final step in photocatalyst preparation before the storage and further application in photocatalytic activity test.

### 2.2 Characterization of photocatalyst

Various analyses to observe the physical and chemical properties of the synthesized photocatalyst were carried out. Phase transformation analysis of the photocatalyst was carried out using thermogravimetric/differential thermal analysis (TG/DTA) (Pyris Diamond TG/DTA, Perkin Elmer) under controlled temperature and heating rate in the range of  $50$ – $850^\circ\text{C}$  and  $10^\circ\text{C min}^{-1}$ , respectively.

Determination of the dominant crystalline phase was observed with X-ray powder diffraction spectroscopy (XRD) (Rigaku X-ray Diffraction Model D/MAS IIIV).

Detailed information of crystal structures was analyzed by MDI Jade 5.0. XRD analysis was carried out using Cu K $\alpha$  radiation in the range of 5–80° with a scan rate of 2° min<sup>-1</sup>. Estimation of the particle sizes and interplanar distance of the photocatalyst were calculated by the Scherrer equation and Bragg's law. Furthermore, to support the crystallite properties analysis, Raman spectroscopy (Tokyo Instruments, Nanofinder 30) was also applied for the determination of degree ordering and crystallinity.

Porous properties and specific surface area analysis were observed using Brunauer-Emmet-Teller (BET) analysis using nitrogen multilayer adsorption method. Scanning electron microscopy (SEM) (JEOL JSM-6700F) was used for the photocatalyst surface properties and transmission electron microscopy (TEM) (JEOL-2100F CS STEM) was used to analyze the crystal structure through its diffraction pattern.

The molecular structure of the chemical functional groups of organic compounds in the photocatalyst was observed using Fourier transform infrared spectroscopy (FTIR) (Perkin Elmer Spectrum One B) equipped with a KBr beam splitter. Deeper observation on the photocatalyst band gap was carried out by the UV-Visible spectrometry (Lambda 35, Perkin Elmer) equipped with an integrating sphere. Analysis was carried out at room temperature and the standard atmospheric air pressure with the wavelengths range of 250–700 nm was set. Furthermore, an X-ray photoelectron spectroscopy (XPS) (ULVAC-PHI 500 Versa Probe ESCA) with the Al K $\alpha$ -radiation (1486 eV) as the source was used for the observation of the binding energy analysis with the calibration reference of C 1s at 285 eV.

### 2.3 Synthesized photocatalyst for the degradation of toluene

Photocatalytic degradation study was carried out in the plug flow reactor system under the temperature of 25 °C, 60% relative humidity (RH), 30 s resident time, and 2.0 ppm initial toluene concentration as the targeted pollutant. Toluene was supplied in a simulated gas system that consist of a mixer, cylinders, and syringe pump with the air (O<sub>2</sub>:N<sub>2</sub> = 21:79) for the purging process.

Synthesized photocatalyst (0.5 g) mixed with 10 mL anhydrous alcohol under continuous stirring for 24 h before coated on the inner surface of a pyrex glass reaction tube with the size of 15.5 cm length, 7.5 cm interior diameter, and 0.5 cm thickness. The oven-drying process will be applied to the pyrex tube with a temperature of 20 °C and installed in the plug flow reactor system. In order to create a firm reactor setup and prevent the leakage or interference from the other light source,

the reactor was placed in a stainless-steel structure. Vaporized toluene was supplied to be photocatalytic degraded by the synthesized photocatalyst using a commercial fluorescent lamp (FL-10D, 10 W, wavelength range of 360–700 nm with a peak  $\lambda = 436$  nm and the light intensity was 2.5 mW cm<sup>-2</sup>) as the light source in the middle of pyrex tube. Light intensity was measured using a luciferase spectrometer (Jasco FP-6200). The concentration of toluene was monitored online using gas chromatography-flame ionization detector during the photo-degradation process.

Photocatalyst with the best toluene degradation performance will be further applied in the photocatalytic activity under various environmental conditions, including initial toluene concentration (1.0–4.0 ppm), temperature (25–45 °C), resident time (5–30 s), and RH (5–80%). Due to the detection limitation in the FTIR instrument, during the experimental study for photocatalytic performance, molecular analyzer (AGM 4000, JSD131108–1) was applied for the CO<sub>2</sub> measurement with the detection limit of 1%.

In the kinetics study, the Langmuir-Hinshelwood kinetic models (Table 4) were applied for the determination of rate constants and adsorption equilibrium constants followed by fitting experimental data using polymath 6.10 software. The value from best fitted model would be applied in the determination of reaction rate constant under the effect of temperature using Arrhenius equation according to the following formula:

$$K = k' \exp\left(-\frac{E_a}{RT}\right) \quad (1)$$

where  $k'$  is the temperature-independent rate constant (mol cm<sup>-3</sup> s<sup>-1</sup>),  $E_a$  is the activation energy (kJ mol<sup>-1</sup>),  $R$  is the gas constant (kJ mol<sup>-1</sup> K<sup>-1</sup>), and  $T$  is the temperature (K).

Moreover, under the assumption of (i) the temperature-dependent of the Langmuir adsorption constant can be used to determine the monolayer adsorption on a homogenous surface and (ii) the rate constant exhibits a temperature dependence that follows the Arrhenius law, therefore, the temperature dependent adsorption constant can be determined according to the following formula:

$$K = K' \frac{\exp\left(-\frac{\Delta H}{RT}\right)}{\sqrt{T}} \quad (2)$$

where  $K$  is the adsorption equilibrium constant (cm<sup>3</sup> mol<sup>-1</sup>),  $K'$  is the temperature-independent adsorption equilibrium constant (K<sup>1/2</sup> cm<sup>3</sup> mol<sup>-1</sup>), and  $\Delta H$  is the enthalpy change of reactants (kJ mol<sup>-1</sup>).

### 3 Results and discussions

#### 3.1 Photocatalyst properties

Analysis of crystallite properties using XRD was presented in Fig. 1a and Table 1 along with supportive data in Fig. S2. A wide peak at around 25.5° indicates the presence of rGO. Moreover, the production of rGO via

solvothermal method was also noticed by the disappearance of the (0 0 2) plane at 11.1° [14]. The peaks located at 25.3, 36.9, 37.8, 48.0, 53.9, 55.1, 62.7, 68.8, 70.3 and 75.0° can be indexed to the (1 0 1), (1 0 3), (0 0 4), (2 0 0), (1 0 5), (2 1 1), (2 0 4), (1 1 6), (2 2 0) and (2 1 5) crystal planes, respectively, of the anatase TiO<sub>2</sub>. However,

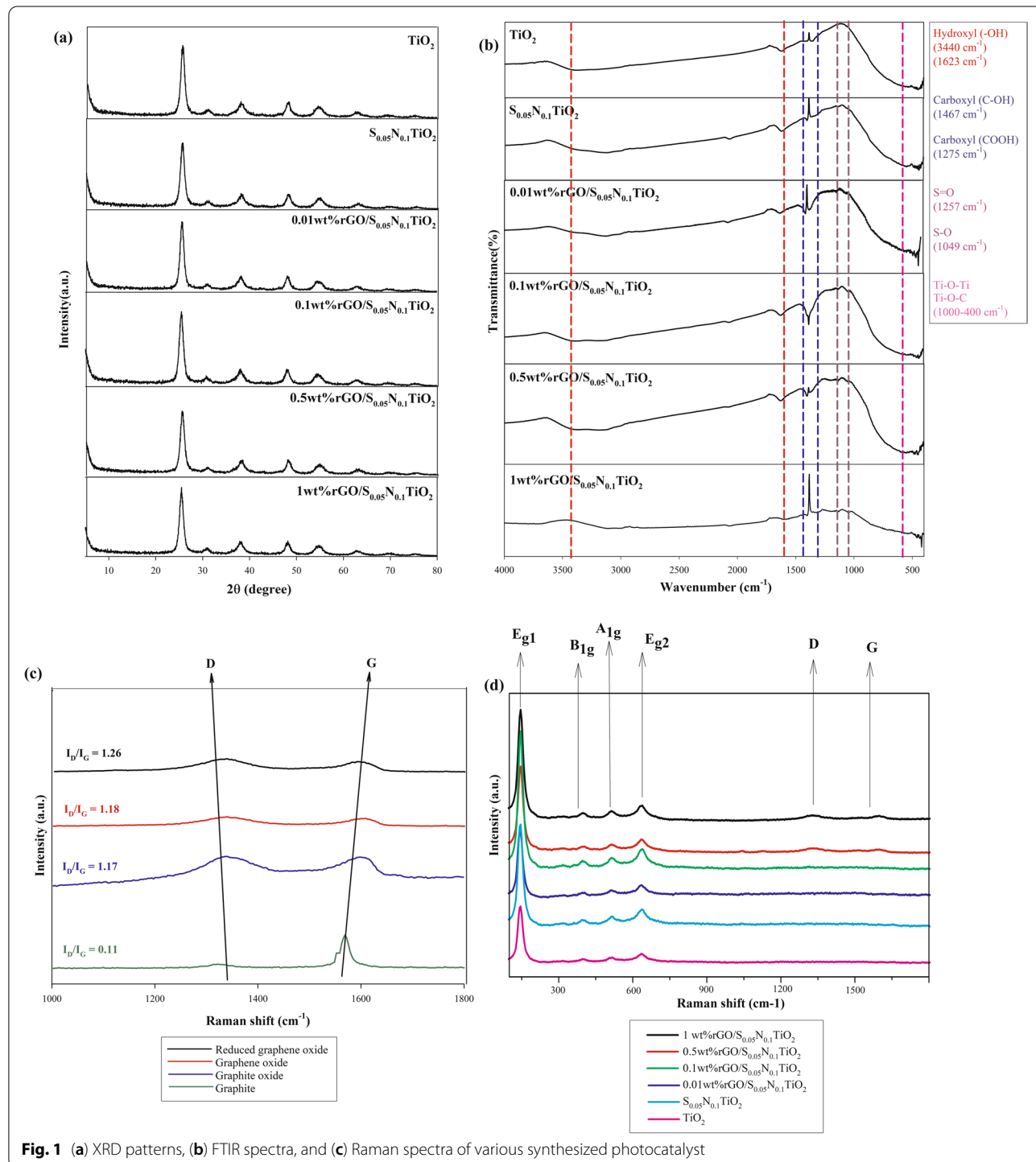


**Fig. 1** (a) XRD patterns, (b) FTIR spectra, and (c) Raman spectra of various synthesized photocatalyst

**Table 1** XRD, Raman, and BET analyses results for the characterization of crystal, bandgap, and pores

Sample	XRD										Raman				BET			
	Crystal phase	Particle size	Crystallite size	Lattice parameter			Absorbance Spectra		Reflectance Spectra		$I_b/I_g$	Surface area ( $m^2 g^{-1}$ )	Pore volume ( $cm^3 g^{-1}$ ) <sup>a</sup>	Pore size (nm) <sup>b</sup>				
				Anatase (%)	D (nm)	d (nm)	a (Å)	c (Å)	c/a	Band gap (eV)					Band edge wavelength (nm)	Band gap (eV)	Band edge wavelength (nm)	
TiO <sub>2</sub>	100	10.45	0.3494	3.771	9.373	2.486	3.19	389	2.55	486	N.D.	155	0.297	7.64				
S <sub>0.05</sub> N <sub>0.1</sub> TiO <sub>2</sub>	100	10.47	0.3498	3.776	9.374	2.483	3.06	405	2.54	488	N.D.	169	0.283	6.68				
0.01wt%rGO/S <sub>0.05</sub> N <sub>0.1</sub> TiO <sub>2</sub>	100	10.60	0.3498	3.778	9.437	2.498	3.03	410	2.53	490	N.D.	149	0.288	7.73				
0.1wt%rGO/S <sub>0.05</sub> N <sub>0.1</sub> TiO <sub>2</sub>	100	10.55	0.3494	3.779	9.431	2.495	2.95	420	2.52	492	N.D.	162	0.297	7.35				
0.5wt%rGO/S <sub>0.05</sub> N <sub>0.1</sub> TiO <sub>2</sub>	100	10.11	0.3502	3.780	9.410	2.489	2.76	450	2.51	494	1.16	161	0.289	7.19				
1wt%rGO/S <sub>0.05</sub> N <sub>0.1</sub> TiO <sub>2</sub>	100	11.11	0.3490	3.773	9.388	2.488	2.73	455	2.50	496	1.43	143	0.276	7.70				

<sup>a</sup> Total pore volume of pores at P/Po=0.99 for single point adsorption; <sup>b</sup> Average pore width (4V/A by BET)

N.D.: not detected

the overlap characteristic peak (002 plane) of rGO at 25° with 101 plane reflection of bare TiO<sub>2</sub> and rGO/TiO<sub>2</sub> at around the same 2θ value creates the almost coincident diffraction patterns [15]. Moreover, no sulfur phase or S containing compounds in the sample with S element in XRD pattern was observed due to the small amount of doping. The particle sizes of S, N, and graphene doped TiO<sub>2</sub> vary with various doping amounts. However, the lattice parameters *a* and *c* remain constant. It indicates that photocatalytic properties of the nanoparticles and charge balance in the anatase lattice are not affected by the dopant presence [16].

Figure 1b displays the FTIR spectra results with the peak appearance at 1650 cm<sup>-1</sup> due to the C=C stretch of alkenes. The presence of TiO<sub>2</sub> can be indicated by the slope between 500 and 1000 cm<sup>-1</sup> due to a Ti-O-Ti vibration. The chemical bond between rGO and TiO<sub>2</sub> nanoparticles created a peak around 793 cm<sup>-1</sup> due to the vibration of Ti-O-C bond, thus, large range from the vibration of Ti-O-Ti and Ti-O-C are hardly distinguished [15]. The stretching mode of S=O and stretching vibration of S-O formed the observed peaks at 1257 and 1049 cm<sup>-1</sup>, respectively [17]. However, the presence of bands from the oxygen-functional groups of graphene oxide in the photocatalyst spectra indicates the incomplete reduction of graphite oxide under the solvothermal method [18].

The Raman spectra of the synthesized photocatalyst was displayed in Fig. 1c. In the Raman spectra, the D band at 1350 cm<sup>-1</sup> is assigned to edge or in-plane sp<sup>3</sup> defects and disordered carbon. On the other hand, the in-plane vibration of ordered sp<sup>2</sup>-bonded carbon atoms was presented as the G band at 1600 cm<sup>-1</sup> [19]. Moreover, compared to graphite oxide, the elevation of I<sub>D</sub>/I<sub>G</sub> intensity ratio was detected in the reduced graphene oxide sample due to functional groups removal which led to the structural change [20]. Furthermore, the overall photocatalyst presents a similar characteristic of anatase structured TiO<sub>2</sub> with the Raman peak. The peaks at 144, 398, 515, and 633 cm<sup>-1</sup> can be assigned as E<sub>g1</sub>, B<sub>1g</sub>, A<sub>1g</sub>, and E<sub>g2</sub>, respectively which were presented by the external vibration of the anatase structure. These peaks are also applied as the indicator of anatase phase formation in the photocatalyst [19]. Moreover, according to the supportive Raman result in Table 1, the value of I<sub>D</sub>/I<sub>G</sub> increases when rGO content increases.

Table 1 also presents the porous structure of synthesized photocatalyst using BET analysis. The pore sizes of all photocatalysts are in the range of 6–7 nm, within the range of the mesoporous (2–50 nm). In addition, all photocatalysts can be attributed to the type IV curve and are tended to hysteresis loops [21]. Compared to bare TiO<sub>2</sub>, the BET surface area of the

different weight percent of rGO/S<sub>0.05</sub>N<sub>0.1</sub>TiO<sub>2</sub> samples significantly decreases with increasing rGO content start from the smallest introduction of rGO content (0.01 wt%). Moreover, reduction of surface area is detected from 162 to 143 m<sup>2</sup> g<sup>-1</sup> with the addition of 0.1 to 1.0 rGO wt%. However, compared to the other rGO addition, low surface area of the 0.01 wt% rGO/S<sub>0.05</sub>N<sub>0.1</sub>TiO<sub>2</sub> is detected. Thus, the dominance of TiO<sub>2</sub> component affecting surface area and porosity is indicated by the BET results [22].

The surface properties of synthesized photocatalyst were analyzed using SEM and TEM as displayed in Fig. 2. TiO<sub>2</sub> composites are dispersed on the surface of rGO and some TiO<sub>2</sub> composites enter into the interlayers of rGO (supported in Fig. S1), this structure supports the efficient electron collection through rGO sheets during the synthesis process [23]. Moreover, the calculation results from Scherrer's equation is in accordance with the quasi-spherical shape-like morphology in TiO<sub>2</sub> and S doped TiO<sub>2</sub> nanoparticles with an average size of 10–15 nm [24]. Increasing rGO content in the photocatalyst forms a larger aggregate.

XPS instrument was applied to observe the chemical and electronic states of the elements and chemical bonding on the surface of photocatalysts as shown in Fig. 3. The spin-orbital splitting photoelectrons in the Ti<sup>4+</sup> valence state caused the peaks centered at 458.4 and 464.0 eV corresponding to Ti 2p<sub>3/2</sub> and Ti 2p<sub>1/2</sub>, respectively in the Ti 2p XPS spectra for TiO<sub>2</sub>. Furthermore, the XPS core level analysis of C 1s confirmed the Ti-C bond [25]. In the C 1s spectra, the bonds of C=C, C-C, C-O and -COOH were identified with the signals at 284.5, 285.1, 286 and 288.6 eV, respectively [26]. The O 1s core-level peaks can be observed at 529.7 eV (Ti-O-Ti/ Ti-O-C), 530.2 eV (C=O), 531.5 eV (C-O) and 532.7 eV (O-H), while the carbon materials has oxygen-containing species at 531.6 eV (-C(=O)-). The Ti-S and C-S bonds are indicated with peaks at 168.3 and 169.3 eV in the S 2p spectra. Moreover, the doping of nitrogen atoms in the anatase lattice which leads to the replacement of a small portion of oxygen atoms through solvothermal process was indicated by the peak at 400.2 eV in the N 1s spectra. Hence, the presence of co-doped N and S on the lattices of rGO/TiO<sub>2</sub> photocatalysts is clearly confirmed by the XPS results [27].

The TG/DTA curves for the synthesized photocatalysts was presented in Fig. 4. In the range of 180 to 380 °C, about 9.0% of weight is lost from TiO<sub>2</sub> due to the organic compound decomposition. The conversion of amorphous precursor into the anatase phase occurred as the temperature increased from 425 to 500 °C. No observed weight loss above 500 °C along with the disappearance of TGA, DTA curves with the higher temperature was observed

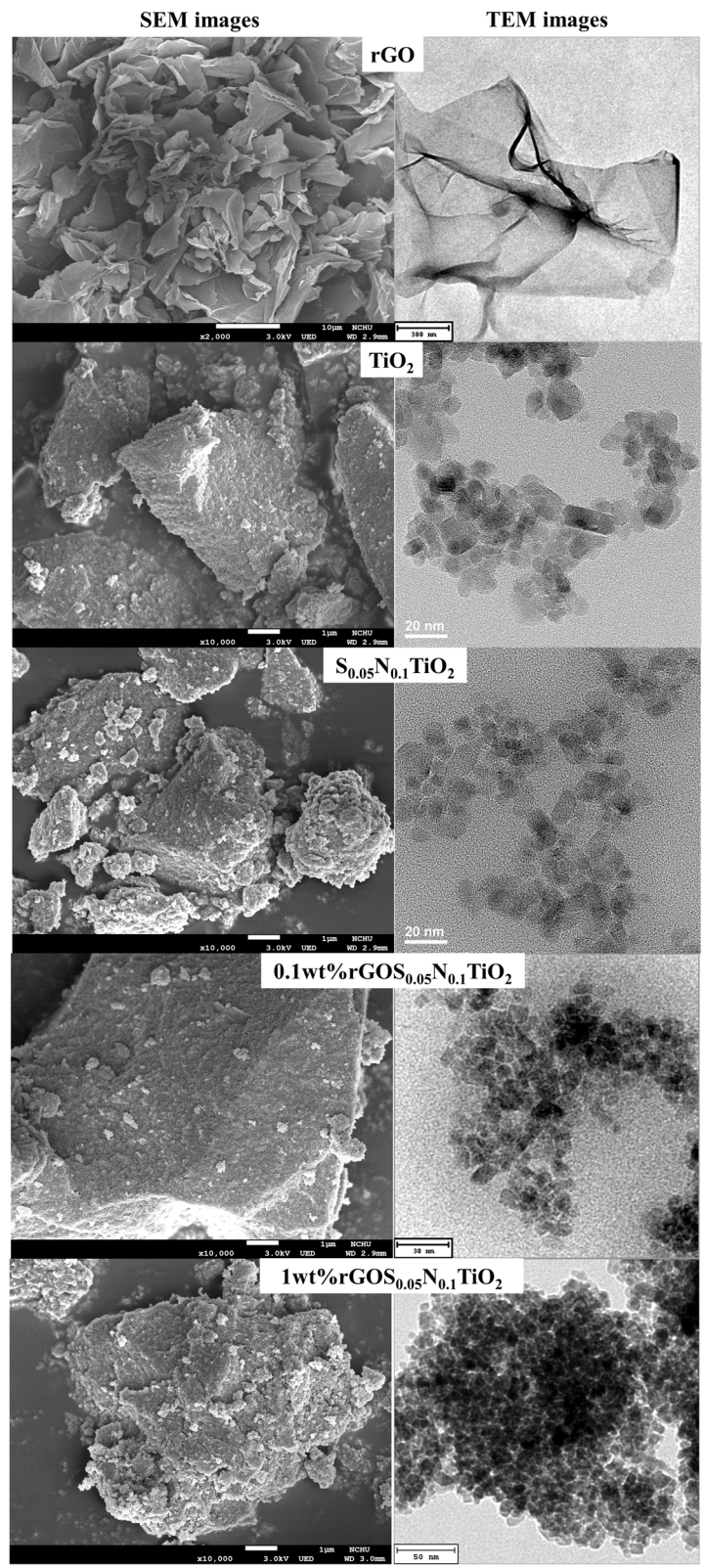
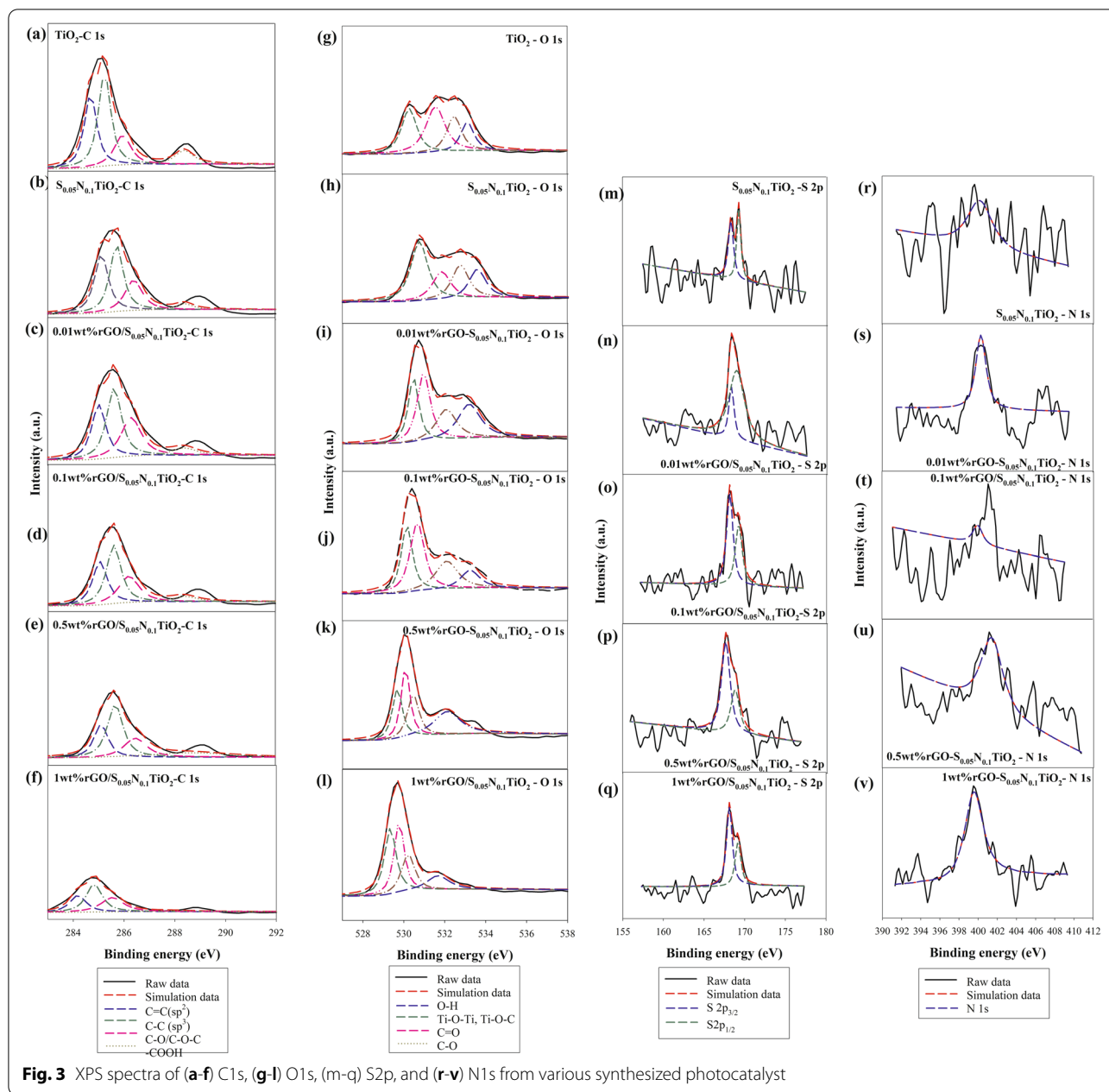


**Fig. 2** The SEM and TEM images of various materials and synthesized photocatalyst



and indicated the initial formation of oxide and the crystal change.

The weight loss in the sample of  $S_{0.05}N_{0.1}TiO_2$  occurs at a temperature range of 50 to 140 °C due to the vaporization of adsorbed/absorbed  $H_2O$  and organics. The removal of strong bonding of water of surface hydroxyl groups causes the 10% weight loss in the range of 150–450 °C in the second region. Moreover, the mass loss due to the S element oxidation was detected in the temperature of 450–800 °C and

followed by the stable value of the remaining weight [28]. However, the photocatalyst with rGO has a higher weight loss than that without rGO in temperature ranges of 150–250 and 600–730 °C. The decomposition of remaining organic compounds formed during the synthesis and partial oxygen-containing functional groups in the rGO causes the weight loss, between 200 and 450 °C. Furthermore, the oxidation of carbon scaffold of the rGO was described by the weight loss in the range of 450–650 °C [29].

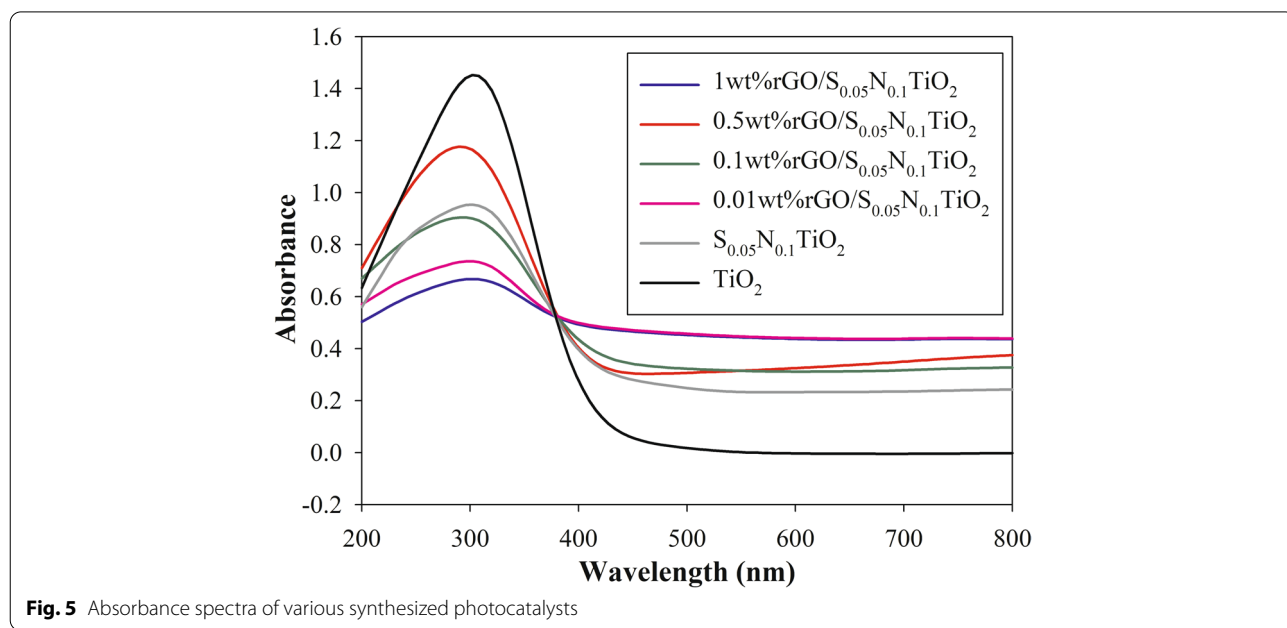
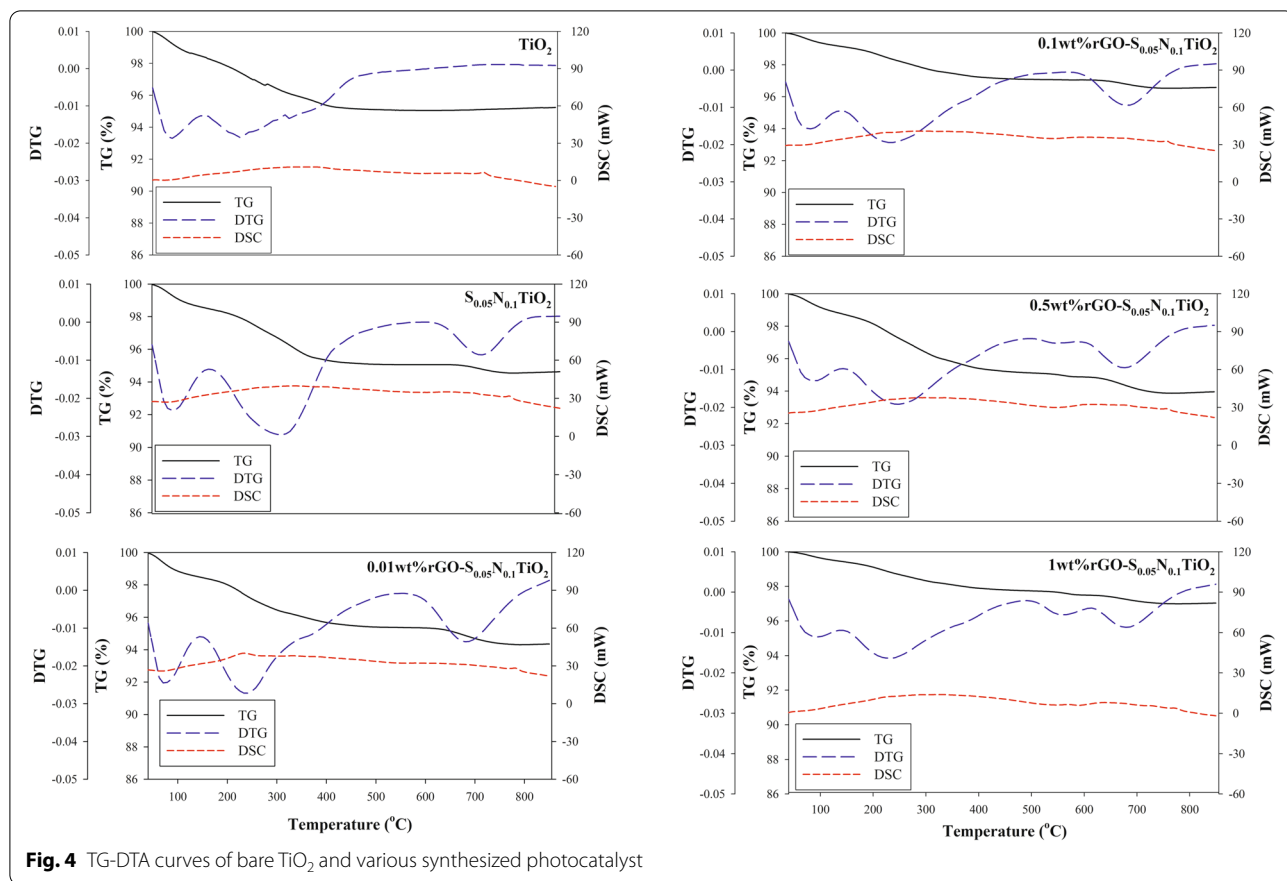


Figure 5 and Fig. S3 display the optical properties of photocatalyst as the result from UV-Visible spectrometry analysis along with the Table 2 for the direct and indirect band-gap. Compared to bare TiO<sub>2</sub>, a noticeable shift of absorption edge was demonstrated by the S, N-doped

TiO<sub>2</sub> samples [15]. The active photocatalytic activity of rGO/S<sub>0.05</sub>N<sub>0.1</sub>TiO<sub>2</sub> composites might occur under visible irradiation with the incident wavelengths in the range 200–800 nm [30]. Estimation of the band gap energies was calculated by reflectance spectra conversion to absorption Kubelka-Munk units as shown in Table 2 and reveal the reduction of energy gap under the higher rGO content. This phenomenon occurred due to the Ti-O-C bonds of rGO/TiO<sub>2</sub> nanocomposites between TiO<sub>2</sub> nanoparticles and rGO nanosheets [15].

**Table 2** Direct and indirect bandgap of the samples from the analysis of UV-Visible spectrophotometer data

Sample	Bandgap (eV)	
	Indirect	Direct
TiO <sub>2</sub>	2.28	3.03
S <sub>0.05</sub> N <sub>0.1</sub> TiO <sub>2</sub>	2.42	3.19
0.01wt%rGO/S <sub>0.05</sub> N <sub>0.1</sub> TiO <sub>2</sub>	2.53	3.17
0.1wt%rGO/S <sub>0.05</sub> N <sub>0.1</sub> TiO <sub>2</sub>	2.44	3.11
0.5wt%rGO/S <sub>0.05</sub> N <sub>0.1</sub> TiO <sub>2</sub>	2.47	3.09
1wt%rGO/S <sub>0.05</sub> N <sub>0.1</sub> TiO <sub>2</sub>	2.56	2.95

### 3.2 Visible light-driven photocatalytic degradation of toluene

Toluene in the initial concentration of 2 ppm was used as the pollutant to be degraded by various synthesized photocatalyst under the RH of 60% at the temperature of 25 °C. Figure 6 and Table 3 present the toluene conversion and reaction rate during photocatalytic degradation. The results indicate that

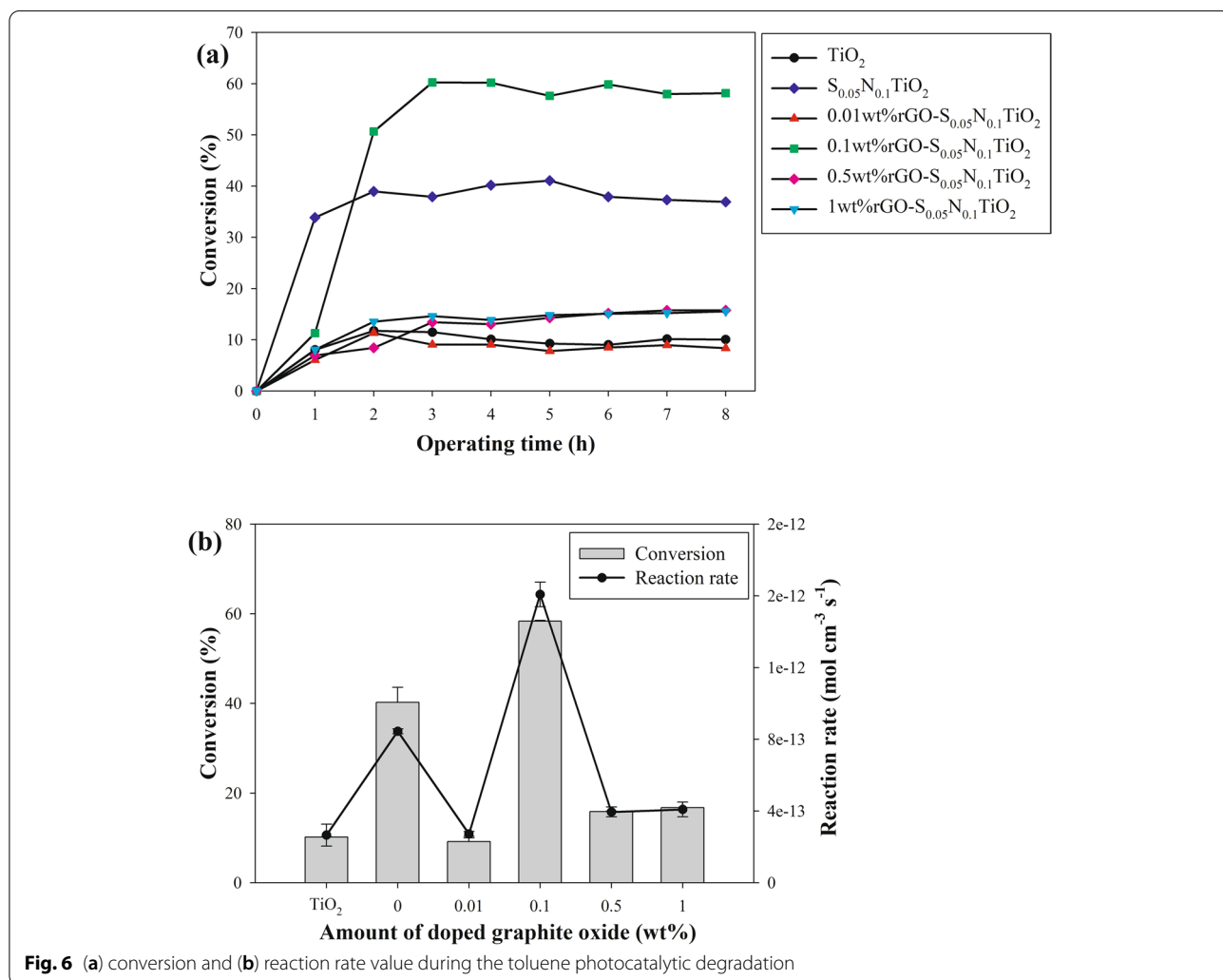


**Fig. 6** (a) conversion and (b) reaction rate value during the toluene photocatalytic degradation

**Table 3** Conversion and the retention time during photocatalytic degradation study under various applied conditions

Photocatalyst	Toluene conc. (ppm)	Temp (°C)	RH (%)	RT (s)	Conversion (%)	Reaction rate (mol cm <sup>-3</sup> s <sup>-1</sup> )					
Various photocatalyst types											
TiO <sub>2</sub>	2 ± 0.5	25	60	30	10.2 ± 0.2	2.66E-13					
S <sub>0.05</sub> N <sub>0.1</sub> TiO <sub>2</sub>					40.3 ± 3.3	8.45E-13					
0.01wt%rGO/S <sub>0.05</sub> N <sub>0.1</sub> TiO <sub>2</sub>					9.2 ± 0.8	2.72E-13					
0.1wt%rGO/S <sub>0.05</sub> N <sub>0.1</sub> TiO <sub>2</sub>					58.3 ± 0.2	1.61E-12					
0.5wt%rGO/S <sub>0.05</sub> N <sub>0.1</sub> TiO <sub>2</sub>					15.9 ± 0.1	3.95E-13					
1wt%rGO/S <sub>0.05</sub> N <sub>0.1</sub> TiO <sub>2</sub>					16.8 ± 1.2	4.09E-13					
Various toluene concentration											
0.1wt%rGO/S <sub>0.05</sub> N <sub>0.1</sub> TiO <sub>2</sub>	1 ± 0.3	25	60	30	69.6 ± 1.6	1.40E-12					
	2 ± 0.2				57.8 ± 3.9	1.38E-12					
	4 ± 0.3				50.7 ± 5.1	2.64E-12					
Various relative humidity											
0.1wt%rGO/S <sub>0.05</sub> N <sub>0.1</sub> TiO <sub>2</sub>	2 ± 0.3	25	0	30	85.0 ± 0.6	2.60E-12					
			1		86.7 ± 0.1	2.64E-12					
			5		76.5 ± 2.7	1.80E-12					
			10		70.6 ± 1.8	1.58E-12					
			30		64.2 ± 2.0	1.39E-12					
			60		58.6 ± 1.6	1.17E-12					
0.1wt%rGO/S <sub>0.05</sub> N <sub>0.1</sub> TiO <sub>2</sub>	2 ± 0.3	25	80	30	44.6 ± 1.0	1.10E-12					
			Various temperature								
			0.1wt%rGO/S <sub>0.05</sub> N <sub>0.1</sub> TiO <sub>2</sub>		2 ± 0.3	25	60	30	57.4 ± 1.3	1.86E-12	
									35	64.2 ± 1.0	2.14E-12
									45	74.0 ± 0.6	2.53E-12
			Various retention time								
0.1wt%rGO/S <sub>0.05</sub> N <sub>0.1</sub> TiO <sub>2</sub>	2 ± 0.2	25	60	5	38.5 ± 1.3	6.50E-12					
				10	43.3 ± 1.1	3.35E-12					
				15	48.8 ± 0.0	2.15E-12					
				30	58.3 ± 0.6	1.57E-12					

0.1wt%rGO/S<sub>0.05</sub>N<sub>0.1</sub>TiO<sub>2</sub> has the best photocatalytic activity among all rGO doping ratios. It is found that co-doped nitrogen and sulfur (N, S) would increase the conversion due to an increase in the absorption of visible light [31]. The presence of additional rGO content promotes the creation of •OH radicals and the interference in •O<sub>2</sub><sup>-</sup> radicals which further lead to the improvement of photocatalytic activity [31]. However, adding excessive or less rGO may increase collision opportunities between electrons and holes which causes faster electron-hole pairs recombination [32]. According to the results, 0.1wt%rGO/S<sub>0.05</sub>N<sub>0.1</sub>TiO<sub>2</sub> will be further implemented for the study of influencing parameters and kinetic analysis.

### 3.3 Photocatalytic activity under various environmental conditions

Photocatalyst with the composition of 0.1wt%rGO/S<sub>0.05</sub>N<sub>0.1</sub>TiO<sub>2</sub> was chosen for the parameters test under various initial toluene concentrations (1–4 ppm), temperature (25–45 °C), RH (0–80%), and retention time (5–30 s). The results of toluene conversion under various parameters are displayed in Fig. 7 along with the data in Table 3. The toluene degradation efficiency was reduced under the supply of higher initial pollutant concentration as seen in Fig. 7a and b. The relationship between pollutant concentration and reaction rate may follow the Langmuir-Hinshelwood model [33], and considering principles of catalytic reactions, at low pollutant

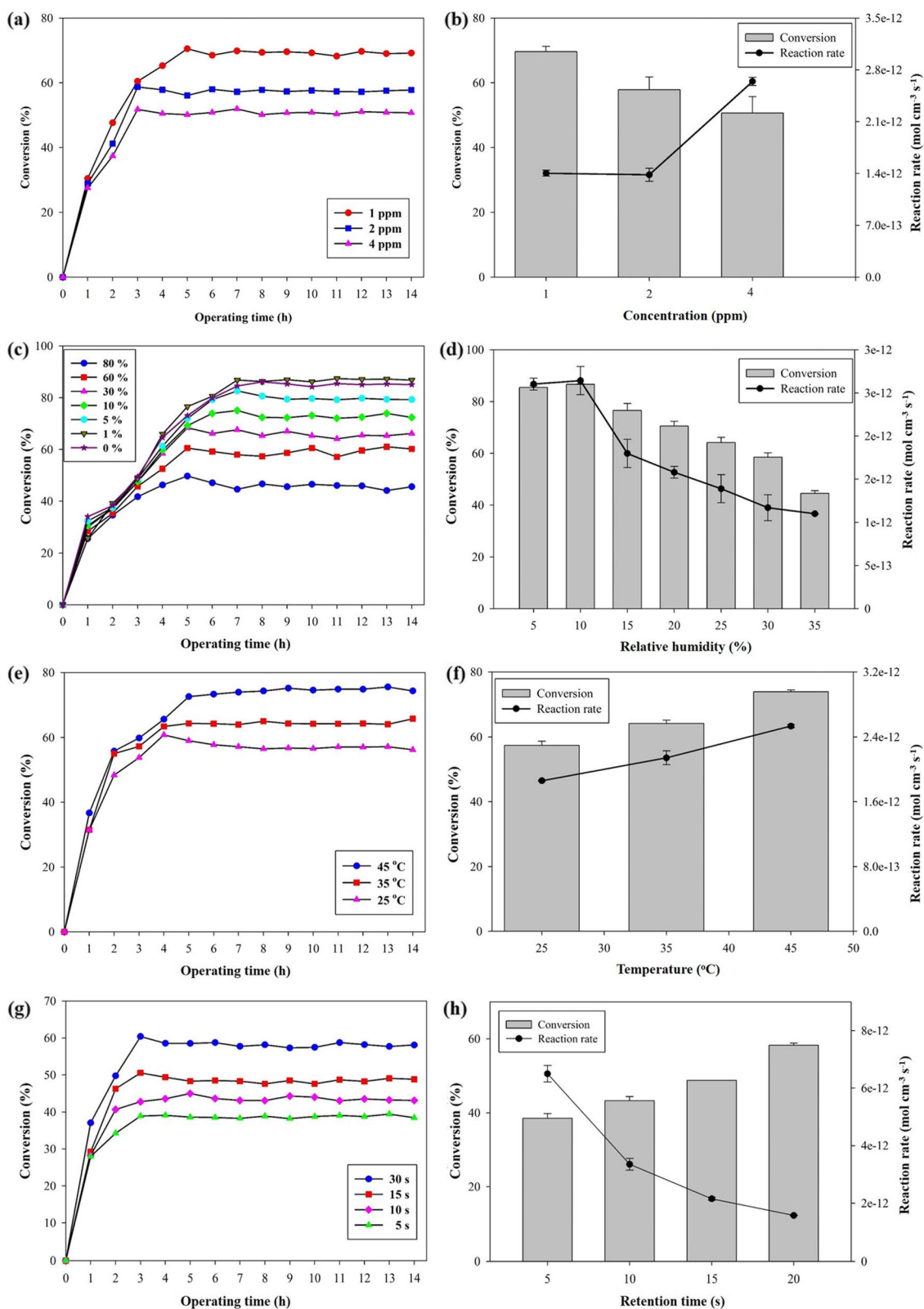


**Fig. 7** Photocatalytic degradation of toluene under various (a, b) initial concentration, (c, d) relative humidity/RH, (e, f) temperature, and (g, h) retention time

concentration, the reaction rate increases with pollutant concentration until it reaches a region where the reaction rate becomes independent of concentration. However, the deposition of refractory reaction intermediates on photocatalyst surface, the loss of active sites, and the dramatic reduction of reaction rate were triggered by the application of high pollutant concentration [34]. The improvement of reaction rate occurred at higher VOC concentration, but the reduction of removal efficiency and mineralization also appeared [34].

Moreover, higher RH value reduced the photocatalytic activity for toluene degradation. The water vapor content in the gaseous effluent created competitive adsorption with toluene molecules on the photocatalyst active sites [35]. However, compared to 0% RH, the higher conversion was detected under the condition of 1% RH which indicated the induction of photocatalytic activity by water vapor due to the hydroxyl radical formation [34].

Under the higher temperature, toluene photocatalytic degradation was also increased due to the exothermic and equilibrium reaction in elementary steps with enhanced the overall reaction rate [36]. Besides the influence on reaction kinetics, higher operating temperature also affects the adsorption of the gas-phase compounds and lowers the amount of adsorbed pollutants on the surface. Thus, the mass transfer might limit the process and cause the lower reaction rate [33]. According to previous study, the optimum temperature was found in the range of 40–50°C. Under low temperature, products desorption will occur due to the slower reaction than the degradation on the surface or the adsorption of reactants. Nevertheless, the higher temperature also becomes a limitation in the toluene adsorption process on the photocatalyst surface [37].

Figure 7g and h display the conversion and reaction rate of the photocatalyst under various retention times. These results indicate the important role of mass transfer and the limitation on oxidation rate due to the direct effect of flow rates on the retention time. The reduction of pollutant's photocatalytic decomposition occurred under higher flow rates and the shorter retention time [38]. The results show that the conversion of toluene increases with an increase in retention time. Reduction of VOC molecules residence time due to the higher air-flow rate ignites the lower adsorption and conversion of the pollutant [34]. However, the reaction rate decreases with an increase in retention time. Therefore, the reduction of residence time raises the importance of adsorption capacity during the reaction [39].

### 3.4 Photocatalytic kinetics analysis

In this study, L-H models 1–7 (Table 4) were used to simulate data generated from the kinetic experimental set

along with the simulation results after the fitting process with polymath software. The simulation results of model 4 are best suited to this study. Under the implementation of higher temperature, the elevation of rate constant  $k$  of model 4 and reduction of adsorption constant  $K_w$  were detected. This phenomenon might occur due to the induction of higher temperature on the species desorption from the surface of photocatalyst. Therefore, the final apparent reaction rate was impacted by the relationship of photocatalytic degradation to both reaction and adsorption constant [40]. Moreover, when the value of  $K_w$  is higher, the pollutant of toluene is more competitive with water.

Table 5 presents the reaction rate constant and adsorption equilibrium constant from the calculation using Arrhenius equation using the values from model 4. The value of reaction rate constant ( $k'$ ) in this study is  $3.15 \times 10^{-7} \text{ mol cm}^{-3} \text{ s}^{-1}$ . Furthermore, the adsorption equilibrium constant for toluene ( $K'_A$ ) and water ( $K'_W$ ) are  $7.46 \times 10^7$  and  $3.52 \times 10^6 \text{ K}^{0.5} \text{ cm}^3 \text{ mol}^{-1}$ , respectively. The dependency of photocatalytic degradation rate on the temperature was represented by the activation energy value ( $10.3 \text{ kJ mol}^{-1}$ ) and created the possibility of surface adsorption–desorption phenomena [41]. Moreover, in this study, the enthalpy value of physisorbed toluene and water are  $-5.3$  and  $-4.5 \text{ kJ mol}^{-1}$ , respectively. These results were supported by the 3D surface mesh diagram as shown in Fig. 8 which presented the well fitted data with the model 4.

### 3.5 Mechanism of toluene photocatalytic degradation

Generated byproduct analysis during the photocatalytic degradation of toluene under 0 and 60% RH using 0.1wt%rGO/S<sub>0.05</sub>N<sub>0.1</sub>TiO<sub>2</sub> for 8 h is shown in Fig. 9 along with the mineralization efficiency curve. The C-H stretching vibration of aromatic ring created the bands at 3076 and 3037  $\text{cm}^{-1}$ . On the other hand, the presence of symmetric and asymmetric C–H stretching vibrations of methyl groups form the bands at 2937 and 2881  $\text{cm}^{-1}$ , respectively. The bands at the range of 1000–1260  $\text{cm}^{-1}$  are corresponding to C–O stretching vibration. In addition, the vibration of aromatic ring is associated with bands at 1609 and 1496  $\text{cm}^{-1}$  [42]. Upon irradiation, the two bands at 2360 and 2338  $\text{cm}^{-1}$  corresponding to CO<sub>2</sub> increase obviously. However, some intermediate products also form in the progress of photocatalytic reaction under visible-light irradiation. The stretching vibration of the aldehydes forms the bands at 1685 and 1671  $\text{cm}^{-1}$  which also indicates the generation of benzaldehyde [43]. Furthermore, the bands located at 1541 and 1508  $\text{cm}^{-1}$  were formed by the stretching vibrational (C=O) of carbonyl compounds in benzaldehyde. For the benzoic acid case, C=C stretching vibration was related with

**Table 4** The calculation results for Langmuir-Hinshelwood models 1–7

Model	Reaction Rate Expression	Temp (K)	k (mol cm <sup>-3</sup> s <sup>-1</sup> )	K <sub>A</sub> (cm <sup>3</sup> mol <sup>-1</sup> )	K <sub>W</sub> (cm <sup>3</sup> mol <sup>-1</sup> )	RSS	R <sup>2</sup>
1	$-r = kx \frac{K_A C_A}{1 + K_A C_A}$	298	2.75E-10	1.02E+08	–	3.62E-20	0.92
		308	3.23E-10	9.89E+07	–	3.37E-20	0.93
		318	4.72E-10	8.30E+07	–	3.12E-20	0.93
2	$-r = kx \frac{K_A C_A K_W C_W}{1 + K_A C_A}$	298	9.41E-02	1.59E+00	1.36E+03	2.87E-23	0.00
		308	4.26E-01	7.18E+00	6.16E+03	9.26E-24	0.35
		318	4.19E-01	7.06E+00	6.05E+03	4.70E-24	0.77
3	$-r = kx \frac{K_A C_A}{1 + K_A C_A + K_W C_W}$	298	9.97E-06	2.34E+03	1.87E+05	1.37E-24	0.89
		308	1.11E-05	2.58E+03	5.99E+04	9.90E-25	0.93
		318	1.29E-05	3.01E+03	7.24E+03	1.34E-24	0.93
4	$-r = kx \frac{K_A C_A K_W C_W}{1 + K_A C_A + K_W C_W}$	298	4.27E-09	3.60E+07	1.25E+06	1.36E-24	0.96
		308	4.81E-09	3.30E+07	1.15E+06	1.68E-24	0.96
		318	5.55E-09	3.05E+07	1.08E+06	1.12E-24	0.95
5	$-r = kx \frac{K_A C_A}{1 + K_A C_A} \times \frac{K_W C_W}{1 + K_W C_W}$	298	2.89E-09	1.00E+07	1.06E+07	9.13E-25	0.93
		308	3.11E-09	1.05E+07	3.06E+07	8.93E-25	0.94
		318	3.49E-09	1.16E+07	1.66E+07	1.27E-24	0.94
6	$-r = Kx \frac{K_A C_A K_W C_W}{1 + K_W C_W}$	298	9.57E-10	1.08E+07	3.02E+07	9.05E-25	0.93
		308	1.02E-09	3.07E+07	3.22E+07	8.93E-25	0.94
		318	1.13E-09	1.67E+07	3.58E+07	1.27E-24	0.94
7	$-rkx \frac{(K_A C_A K_W C_W)^{1/2}}{[1 + (K_A C_A)^{1/2} + (K_W C_W)^{1/2}]^2}$	298	8.16E-09	1.84E+04	6.19E+05	3.76E-24	0.70
		308	9.28E-09	1.89E+04	6.36E+05	4.76E-24	0.67
		318	1.26E-08	1.53E+04	6.35E+05	6.98E-24	0.66

Note: k = reaction rate constant (mol cm<sup>-3</sup> s<sup>-1</sup>); K<sub>A</sub> = toluene adsorption equilibrium constants (cm<sup>3</sup> mol<sup>-1</sup>); K<sub>W</sub> = water vapor adsorption equilibrium constants (cm<sup>3</sup> mol<sup>-1</sup>); r = reaction rate (mol cm<sup>-3</sup> s<sup>-1</sup>); C<sub>A</sub> = toluene concentration (mol cm<sup>-3</sup>); C<sub>W</sub> = water concentration (mol cm<sup>-3</sup>)

**Table 5** The reaction rate constants and adsorption equilibrium constants of Langmuir-Hinshelwood model 4 using Arrhenius equation

Parameters	Units	Model 4
k'	mol cm <sup>-3</sup> s <sup>-1</sup>	3.15E-07
K' <sub>A</sub>	K <sup>0.5</sup> cm <sup>3</sup> mol <sup>-1</sup>	7.46E+07
K' <sub>W</sub>	K <sup>0.5</sup> cm <sup>3</sup> mol <sup>-1</sup>	3.52E+06
E <sub>a</sub>	kJ mol <sup>-1</sup>	10.3
ΔH <sub>A</sub>	kJ mol <sup>-1</sup>	–5.3
ΔH <sub>W</sub>	kJ mol <sup>-1</sup>	–4.5

the peaks centered at 1653 and 1636 cm<sup>-1</sup> while peaks at 1558 and 1521 cm<sup>-1</sup> were the indicators of carboxylate group COO- asymmetric stretching vibration modes. Moreover, the characteristic peaks of benzyl alcohol were indicated by the bands at 1473 and 1457 cm<sup>-1</sup> [31].

At 0% RH, C-H group, CO<sub>2</sub>, and C-O bindings were detected, however, these peaks cannot be found. It is

suggested that toluene may not be converted completely to CO<sub>2</sub> at high RH, and the toluene conversion decreases with an increase of RH. The presence of water content in higher humidity conditions creates competition in the adsorption process toluene on the photocatalyst surface. Therefore, the partially oxidized of toluene species (such as benzaldehyde and benzoic acid) were widely observed under higher humidity conditions and remained on the photocatalyst surface. As reported by Li et al. [44] the generated intermediate products are capable to build complexation with photocatalyst surface and may lead to the deactivation. However, under the dry condition, the early conversion of toluene to CO<sub>2</sub> was detected and the deactivation of photocatalyst was prevented.

For the analysis of mineralization ratio, the experiments were carried out at the retention time of 30s, the inlet concentration of toluene 1 ppm, RH 60%, and ambient temperature 25°C. It can be found that the conversion and mineralization efficiency gradually increase with decomposition time until a steady-state occurs, which indicates that toluene is oxidized into CO<sub>2</sub> and

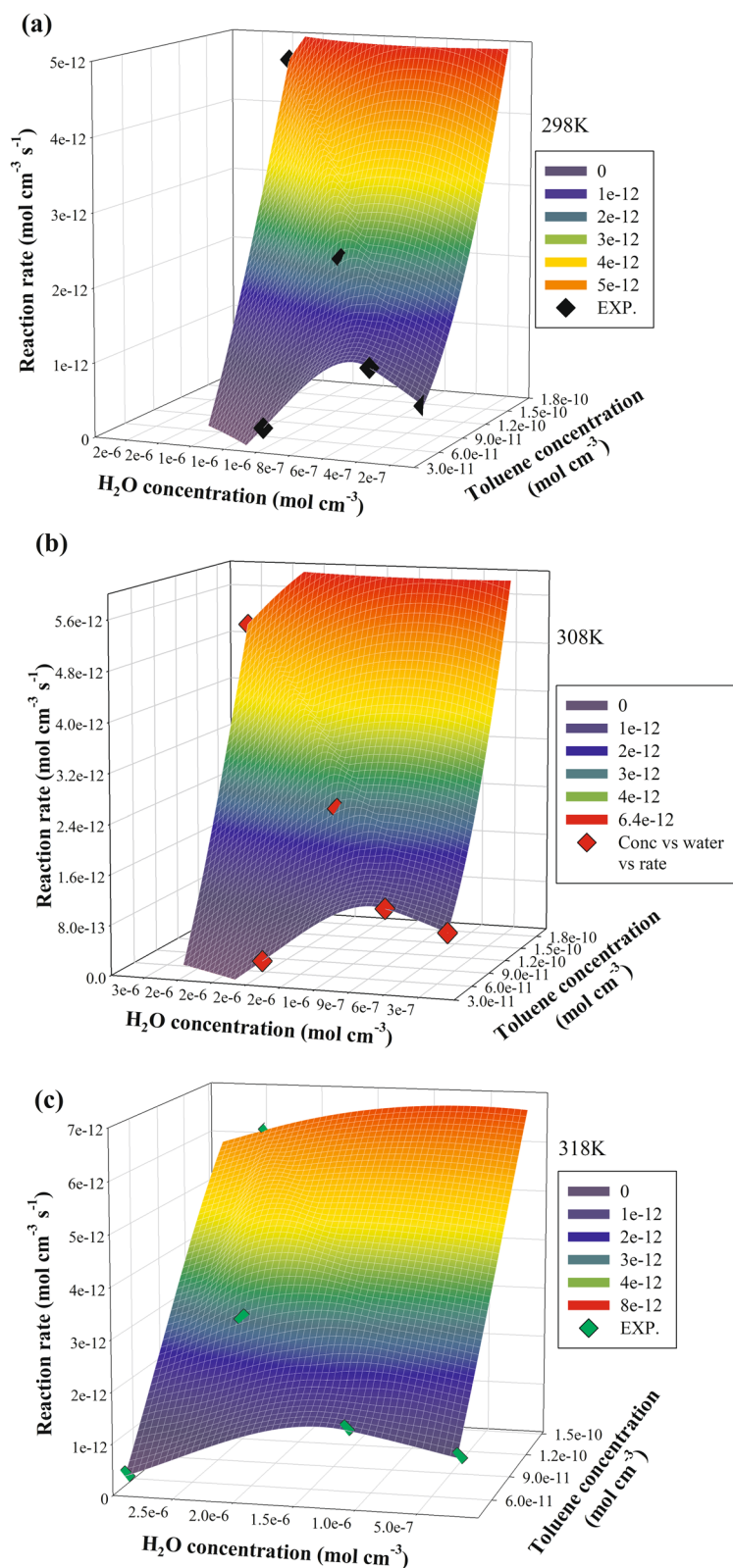


**Fig. 8** The reaction rate predicted and experimental values using Langmuir-Hinshelwood models 4 at (a) 298, (b) 308, and (c) 318K

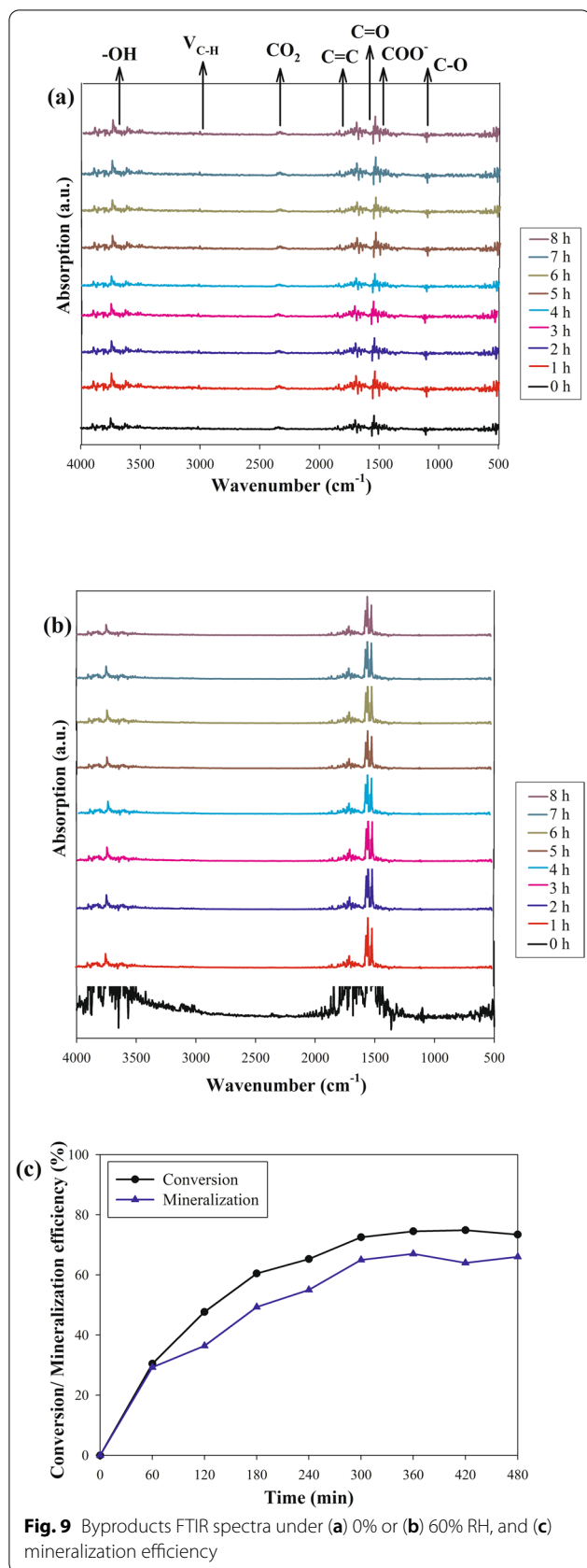


**Fig. 9** Byproducts FTIR spectra under (a) 0% or (b) 60% RH, and (c) mineralization efficiency

H<sub>2</sub>O. However, the conversion of toluene to CO<sub>2</sub> and H<sub>2</sub>O is not 100%, some intermediate products are also formed in the progress of photocatalytic reaction [45]. Nevertheless, the FTIR instrument could not detect the low concentration of CO<sub>2</sub> functional groups due to the incomplete conversion, therefore the detection of CO<sub>2</sub> content was measured by the CO<sub>2</sub> molecular analyzer.

According to the result of FTIR and mineralization analyses along with the previous study of Sleiman et al. [45], the predicted photodegradation mechanism is illustrated in Fig. 10. The reaction between O<sub>2</sub> or H<sub>2</sub>O with the electron and hole generates reactive oxygen species ( $\bullet$ OH and  $\bullet$ O<sub>2</sub><sup>-</sup>) which take part in the photocatalytic reaction. Thus, the photocatalytic oxidation of toluene to benzaldehyde at the beginning of reaction. This result is also supported by the FTIR spectra that display the stretching vibrational (C=O) of carbonyl compounds in benzaldehyde. Under longer irradiation time, further conversion of the benzaldehyde into benzoic acid was achieved and proved by the benzoic acid asymmetric stretching vibration modes of the carboxylate group COO<sup>-</sup> in the FTIR result. Final conversion of toluene into CO<sub>2</sub> and H<sub>2</sub>O reduced its toxicity [46].

Based on the FTIR analysis of generated byproducts (Fig. 9), RH controls two competitive reaction pathways which is related to the different active species that affect the adsorption mode of toluene on photocatalyst surface. An electron transfer process from toluene to TiO<sub>2</sub> initiates the formation of a benzyl radical in the absence of water vapor. The generated benzyl-peroxyl radical from the reaction of benzyl radical with O<sub>2</sub> will be further thermally disintegrated on the surface. Furthermore, the formation of an aromatic bridged peroxy intermediate was related to the reaction of aromatic radical cation with O<sub>2</sub>. Further conversion of benzaldehyde to benzoic acid and followed by the decomposition on the TiO<sub>2</sub> surface elevates the benzene and CO<sub>2</sub> content. The reaction will be completed by a sequence of oxidation reactions by holes, oxygen, and  $\bullet$ OH radicals at a lesser extent which will lead to the final product (CO<sub>2</sub>). Moreover, the accumulation of generated water content also involved in the possibility of competitive adsorption with the contaminant molecules and further reduced the photocatalytic activity performance [47].

#### 4 Conclusions

The modification on TiO<sub>2</sub> photocatalyst was carried out by the addition of rGO and non-metal elements (S, and N). The particle TiO<sub>2</sub> attached to the rGO surface and interposed between the layers which promoted the elevation of specific surface area. Photocatalytic activity improvement was achieved by the formation of chemical defects and bonding which introduces the oxygen-containing

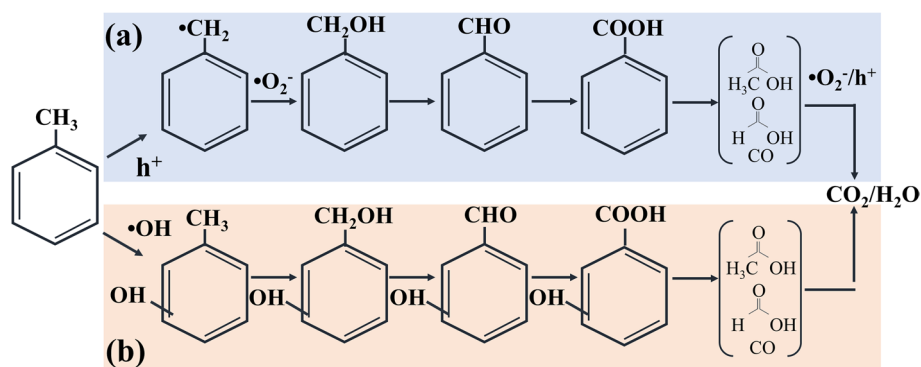


**Fig. 10** Predicted photocatalytic degradation of toluene under (a) 0% RH or (b) 60% RH

functional groups during the process. Moreover, the absorption spectra result of UV-Visible indicated a greater absorption intensity of visible light along with the reduction of bandgap with the addition of S and N elements. The rGO content itself also plays an important role in the electron transport process. However, excess rGO content will inhibit the light absorption, and in this study, 0.1 wt% of rGO is considered as the optimum composition for the addition in the photocatalyst material. RH value also plays an important role in the photocatalytic activity which relates to the competitive adsorption between water and toluene molecules on the photocatalyst surface. Higher collision frequency at higher temperature also enhanced the photocatalytic activity. The suitable kinetic modeling was achieved by the L-H model 4. During the photocatalytic degradation of toluene, the molecules will be converted into benzyl alcohol, benzaldehyde, benzoic acid, and carbon dioxide.

### Supplementary Information

The online version contains supplementary material available at <https://doi.org/10.1186/s42834-022-00143-w>.

#### Additional file 1.

### Acknowledgements

The authors acknowledge appreciatively to the Ministry of Science and Technology, Taiwan, for the financial support on the research with project number of MOST (106-2221-E-006-017-MY3).

### Authors' contributions

Birgitta Narindri Rara Winayu investigated the resources, provided data visualization and original draft writing, review & editing. Wan-Hua Mao provided methodology, resources investigation, data analysis and validation. Hsin Chu supported the conceptualization, methodology, supervision, project administration, funding acquisition, manuscript writing-review and editing. The authors read and approved the final manuscript.

### Funding

This work was supported by Taiwan Ministry of Science and Technology (MOST 106-2221-E-006-017-MY3).

### Availability of data and materials

All data in this study are generated and analyzed by our group during the examination and verification process.

### Declarations

#### Competing interests

The authors declare that they have no known competing financial interests or personal relationships that could have appeared to influence the work reported in this paper.

Received: 24 September 2021 Accepted: 2 June 2022

Published online: 29 June 2022

### References

- McNamara ML, Thornburg J, Semmens EO, Ward TJ, Noonan CW. Reducing indoor air pollutants with air filtration units in wood stove homes. *Sci Total Environ.* 2017;592:488–94.
- Liu JM, Ma FY, Zhu YH, Ye YF, Liang YQ, Liu YE, et al. Hydrodynamic cavitation for the enhancement of toluene disproportionation; study of the products distribution. *Chem Eng Process* 2018;125:34–43.
- Jeon J, Park JH, Wi S, Yun BY, Kim T, Kim S. Field study on the improvement of indoor air quality with toluene adsorption finishing materials in an urban residential apartment. *Environ Pollut* 2020;261:114137.
- Wu H, Guo CY, Yin ZH, Quan Y, Yin CR. Performance and bacterial diversity of biotrickling filters filled with conductive packing material for the treatment of toluene. *Bioresour Technol* 2018;257:201–9.
- MiarAlipour S, Friedmann D, Scott J, Amal R. TiO<sub>2</sub>/porous adsorbents: recent advances and novel applications. *J Hazard Mater* 2018;341:404–23.
- Rahimi N, Pax RA, Gray EM. Review of functional titanium oxides. I: TiO<sub>2</sub> and its modifications. *Prog Solid State Ch* 2016;44:86–105.
- Park JY, Choi KI, Lee JH, Hwang CH, Choi DY, Lee JW. Fabrication and characterization of metal-doped TiO<sub>2</sub> nanofibers for photocatalytic reactions. *Mater Lett* 2013;97:64–6.
- Khaki MRD, Shafeeyan MS, Raman AAA, Daud WMAW. Application of doped photocatalysts for organic pollutant degradation – a review. *J Environ Manage* 2017;198:78–94.
- Fotiou T, Triantis TM, Kaloudis T, O'Shea KE, Dionysiou DD, Hiskia A. Assessment of the roles of reactive oxygen species in the UV and visible light photocatalytic degradation of cyanotoxins and water taste and odor compounds using C-TiO<sub>2</sub>. *Water Res* 2016;90:52–61.
- Zhou Wq, Yu CL, Fan QZ, Wei LF, Chen JC, Yu JC. Ultrasonic fabrication of N-doped TiO<sub>2</sub> nanocrystals with mesoporous structure and enhanced visible light photocatalytic activity. *Chinese J Catal* 2013;34:1250–5.
- Yu CL, Cai DJ, Yang K, Yu JC, Zhou Y, Fan CF. Sol-gel derived S<sub>2</sub>I-codoped mesoporous TiO<sub>2</sub> photocatalyst with high visible-light photocatalytic activity. *J Phys Chem Solids* 2010;71:1337–43.

12. Nalid NR, Majid A, Tahir MB, Niaz NA, Khalid S. Carbonaceous-TiO<sub>2</sub> nano-materials for photocatalytic degradation of pollutants: a review. *Ceram Int* 2017;43:14552–71.
13. Hummers WS, Offeman RE. Preparation of graphitic oxide. *J Am Chem Soc* 1958;80:1339.
14. Kumar KD, Kumar GP, Reddy KS. Rapid microwave synthesis of reduced graphene oxide-supported TiO<sub>2</sub> nanostructures as high performance photocatalyst. *Mater Today-Proc* 2015;2:3736–42.
15. Chen YZ, Li AX, Li Q, Hou XM, Wang LN, Huang ZH. Facile fabrication of three-dimensional interconnected nanoporous N-TiO<sub>2</sub> for efficient photoelectrochemical water splitting. *J Mater Sci Technol* 2018;34:955–60.
16. Burns A, Hayes G, Li W, Hirvonen J, Demaree JD, Shah SI. Neodymium ion dopant effects on the phase transformation in sol-gel derived titania nanostructures. *Mat Sci Eng B-Solid* 2004;111:150–5.
17. Sharotri N, Sud D. A greener approach to synthesize visible light responsive nanoporous S-doped TiO<sub>2</sub> with enhanced photocatalytic activity. *New J Chem* 2015;39:2217–23.
18. Aleksandrak M, Adamski P, Kukulka W, Zielinska B, Mijowska E. Effect of graphene thickness on photocatalytic activity of TiO<sub>2</sub>-graphene nanocomposites. *Appl Surf Sci* 2015;331:193–9.
19. Yadav HM, Kim JS. Solvothermal synthesis of anatase TiO<sub>2</sub>-graphene oxide nanocomposites and their photocatalytic performance. *J Alloy Compd* 2016;688:123–29.
20. Zhang L, Hou GM, Zhai W, Ai Q, Feng JK, Zhang L, et al. Aluminum/graphene composites with enhanced heat-dissipation properties by in-situ reduction of graphene oxide on aluminum particles. *J Alloy Compd* 2018;748:854–60.
21. Hao N, Hua R, Chen SB, Zhang Y, Zhou Z, Qian J, et al. Multiple signal-amplification via Ag and TiO<sub>2</sub> decorated 3D nitrogen doped graphene hydrogel for fabricating sensitive label-free photoelectrochemical thrombin aptasensor. *Biosens Bioelectron* 2018;101:14–20.
22. Zhang YX, Zhou ZY, Chen T, Wang HT, Lu WJ. Graphene TiO<sub>2</sub> nanocomposites with high photocatalytic activity for the degradation of sodium pentachlorophenol. *J Environ Sci-China* 2014;26:2114–22.
23. Dong L, Li MS, Dong L, Zhao ML, Feng JM, Han Y, et al. Hydrothermal synthesis of mixed crystal phases TiO<sub>2</sub>-reduced graphene oxide nanocomposites with small particle size for lithium ion batteries. *Int J Hydrogen Energ* 2014;39:16116–22.
24. Singaram B, Varadarajan K, Jeyaram J, Rajendran R, Jayavel V. Preparation of cerium and sulfur codoped TiO<sub>2</sub> nanoparticles based photocatalytic activity with enhanced visible light. *J Photoch Photobio A* 2017;349:91–9.
25. Ghasemi S, Hashemian SJ, Alamolhoda AA, Gocheva I, Setayesh SR. Plasmon enhanced photocatalytic activity of Au@TiO<sub>2</sub>-graphene nanocomposite under visible light for degradation of pollutants. *Mater Res Bull* 2017;87:40–7.
26. Cong Y, Li XK, Qin Y, Dong ZJ, Yuan GM, Cui ZW, et al. Carbon-doped TiO<sub>2</sub> coating on multiwalled carbon nanotubes with higher visible light photocatalytic activity. *Appl Catal B-Environ* 2011;107:128–34.
27. Appavu B, Thiripuranthagan S. Visible active N, S co-doped TiO<sub>2</sub>/graphene photocatalysts for the degradation of hazardous dyes. *J Photoch Photobio A* 2017;340:146–56.
28. Boningari T, Inturi SNR, Suidan M, Smirniotis PG. Novel one-step synthesis of sulfur doped-TiO<sub>2</sub> by flame spray pyrolysis for visible light photocatalytic degradation of acetaldehyde. *Chem Eng J* 2018;339:249–58.
29. Suave J, Amorim SM, Angelo J, Andrade L, Mendes A, Moreira RFP. TiO<sub>2</sub>/reduced graphene oxide composites for photocatalytic degradation in aqueous and gaseous medium. *J Photoch Photobio A* 2017;348:326–36.
30. Martins PM, Ferreira CG, Silva AR, Magalhaes B, Alves MM, Pereira L, et al. TiO<sub>2</sub>/graphene and TiO<sub>2</sub>/graphene oxide nanocomposites for photocatalytic applications: a computer modeling and experimental study. *Compos Part B-Eng* 2018;145:39–46.
31. Li X, Shen RC, Ma S, Chen XB, Xie J. Graphene-based heterojunction photocatalysts. *Appl Surf Sci* 2018;430:53–107.
32. Xu DF, Li LL, He RA, Qi LF, Zhang LY, Cheng B. Noble metal-free RGO/TiO<sub>2</sub> composite nanofiber with enhanced photocatalytic H<sub>2</sub>-production performance. *Appl Surf Sci* 2018;434:620–5.
33. Mo JH, Zhang YP, Xu QJ, Lamson JJ, Zhao RY. Photocatalytic purification of volatile organic compounds in indoor air: a literature review. *Atmos Environ* 2009;43:2229–46.
34. Mamaghani AH, Haghigat F, Lee CS. Photocatalytic degradation of VOCs on various commercial titanium dioxides: impact of operating parameters on removal efficiency and by-products generation. *Build Environ* 2018;138:275–82.
35. Zadi T, Assadi AA, Nasrallah N, Bouallouche R, Tri PN, Bouzaza A, et al. Treatment of hospital indoor air by a hybrid system of combined plasma with photocatalysis: case of trichloromethane. *Chem Eng J* 2018;349:276–86.
36. Yamamoto A, Mizuno Y, Teramura K, Shishido T, Tanaka T. Effects of reaction temperature on the photocatalytic activity of photo-SCR of NO with NH<sub>3</sub> over a TiO<sub>2</sub> photocatalyst. *Catal Sci Technol* 2013;3:1771–5.
37. Reza KM, Kurny ASW, Gulshan F. Parameters affecting the photocatalytic degradation of dyes using TiO<sub>2</sub>: a review. *Appl Water Sci* 2017;7:1569–78.
38. Tsai CW, Chang CT, Chiou CS, Shie JL, Chang YM. Study on the indoor volatile organic compound treatment and performance assessment with TiO<sub>2</sub>/MCM-41 and TiO<sub>2</sub>/quartz photoreactor under ultraviolet irradiation. *J Air Waste Manage* 2008;58:1266–73.
39. Lv KL, Fang S, Si LL, Xia Y, Ho WK, Li M. Fabrication of TiO<sub>2</sub> nanorod assembly grafted rGO (rGO@TiO<sub>2</sub>-NR) hybridized flake-like photocatalyst. *Appl Surf Sci* 2017;391:218–27.
40. Hu M, Yao ZH, Liu X, Ma LP, He Z, Wang XQ. Enhancement mechanism of hydroxyapatite for photocatalytic degradation of gaseous formaldehyde over TiO<sub>2</sub>/hydroxyapatite. *J Taiwan Inst Chem E* 2018;85:91–7.
41. Parrino F, Conte P, De Pasquale C, Laudicina VA, Loddo V, Palmisano L. Influence of adsorbed water on the activation energy of model photocatalytic reactions. *J Phys Chem C* 2017;121:2258–67.
42. Zhang ZG, Li XY, Liu BJ, Zhao QD, Chen GH. Hexagonal microspindle of NH<sub>2</sub>-MIL-101(Fe) metal-organic frameworks with visible-light-induced photocatalytic activity for the degradation of toluene. *RSC Adv* 2016;6:4289–95.
43. Zhu ZR, Liu FY, Zhang W. Fabricate and characterization of Ag/BaAl<sub>2</sub>O<sub>4</sub> and its photocatalytic performance towards oxidation of gaseous toluene studied by FTIR spectroscopy. *Mater Res Bull* 2015;64:68–75.
44. Li H, Jiang FZ, Drdova S, Shang H, Zhang LZ, Wang J. Dual-function surface hydroxyl bonds enable robust O<sub>2</sub> activation for deep photocatalytic toluene oxidation. *Catal Sci Technol* 2021;11:319–31.
45. Sleiman M, Conchon P, Ferronato C, Chovelon JM. Photocatalytic oxidation of toluene at indoor air levels (ppbv): towards a better assessment of conversion, reaction intermediates and mineralization. *Appl Catal B-Environ* 2009;86:159–65.
46. Li XY, Li JA, Shi Y, Zhang MM, Fan SY, Yin ZF, et al. Rational design of cobalt and nitrogen co-doped carbon hollow frameworks for efficient photocatalytic degradation of gaseous toluene. *J Colloid Interf Sci* 2018;528:45–52.
47. Lin YH, Hsueh HT, Chang CW, Chu H. The visible light-driven photodegradation of dimethyl sulfide on S-doped TiO<sub>2</sub>: characterization, kinetics, and reaction pathways. *Appl Catal B-Environ* 2016;199:1–10.

## Publisher's Note

Springer Nature remains neutral with regard to jurisdictional claims in published maps and institutional affiliations.

**Ready to submit your research? Choose BMC and benefit from:**

- fast, convenient online submission
- thorough peer review by experienced researchers in your field
- rapid publication on acceptance
- support for research data, including large and complex data types
- gold Open Access which fosters wider collaboration and increased citations
- maximum visibility for your research: over 100M website views per year

**At BMC, research is always in progress.**

Learn more [biomedcentral.com/submissions](https://biomedcentral.com/submissions)

